Journal of Glaciology

Article

Cite this article: Sayers CM (2021). Porosity dependence of elastic moduli of snow and firn. *Journal of Glaciology* **67**(265), 788–796. https://doi.org/10.1017/jog.2021.25

Received: 22 August 2020
Revised: 18 February 2021
Accepted: 19 February 2021
First published online: 18 March 2021

Keywords:
Polar firn; snow; snow physics

Author for correspondence:
Colin M. Sayers, E-mail: cmsayers@uh.edu

cambridge.org/jog

Porosity dependence of elastic moduli of snow and firn

Colin M. Sayers

University of Houston, Houston, TX, USA

Abstract

Measurements of elastic wave velocities enable non-destructive estimation of the mechanical properties, elastic moduli and density of snow and firn. The variation of elastic moduli with porosity in dry snow and firn is modeled using a differential effective medium scheme modified to account for the critical porosity above which the bulk and shear moduli of the ice frame vanish. A comparison of predicted and measured elastic moduli indicates that the shear modulus of ice in snow is lower than that computed from single crystal elastic stiffnesses of ice. This may indicate that the bonds between snow particles are more deformable under shear than under compression. A partial alignment of ice crystals also may contribute. Good agreement between elastic stiffnesses of the ice frame obtained from elastic wave velocity measurements and the predictions of the theory is observed. The approach is simple and compact, and does not require the use of empirical fits to the data. Owing to its simplicity, this model may prove useful in a variety of potential applications such as construction on snow, interpretation of seismic measurements to monitor and locate avalanches and estimation of density within compacting snow deposited on glaciers and ice sheets.

Introduction

As snow transforms to ice it passes through an intermediate stage referred to as firn. According to Cuffey and Paterson (2010), snow has density in the range 50–400 kg m^{-3}, while firn has density in the range 400–800 kg m^{-3}. The purpose of this paper is to model the elastic properties of dry snow and firn to help in monitoring the transition from snow to firn and then into ice. Measurements of elastic wave velocities provide a non-destructive method for estimating the mechanical properties, elastic moduli and density of snow and firn (Mellor, 1974; Shapiro and others, 1997). Smith (1965), for example, found a correlation between crushing strength and *P*-wave velocity for naturally compacted snow having densities in the range 390–914 kg m^{-3} from Camp Century on Greenland Ice Cap.

The mechanical properties of snow are of interest for a variety of applications such as construction on snow, snow removal, vehicle mobility and avalanche release and control (Salm, 1982). The elastic properties relate stress and strain, and are needed for the interpretation of seismic measurements, which have been used to monitor and locate avalanches (Suriñach and others, 2005; Van Herwijnen and Schweizer, 2011; Lacroix and others, 2012). Another application is the non-destructive estimation of density as a function of depth within compacting snow deposited on glaciers and ice sheets, as investigated by Schlegel and others (2019) using diving-wave refraction velocity analysis. This enables improved monitoring of the surface mass balance of glaciers and ice sheets using airborne or satellite altimetry by allowing the measured surface elevation over time to be corrected for compaction of snow.

Several authors (e.g. Pieritz and others, 2004; Schneebeli, 2004; Srivastava and others, 2010; Köchle and Schneebeli, 2014; Wautier and others, 2015; Srivastava and others, 2016; Gerling and others, 2017) have used finite element analysis based on the 3-D microstructure of snow reconstructed from microtomography to predict elastic properties. This allows the relation between the computed elastic properties and parameters characterizing the microstructure such as porosity, the ratio of closed to total porosity, pore connectivity, pore surface-to-volume ratio and structure model index to be examined (e.g. Kaempfer and Schneebeli, 2007; Ohser and others, 2009; Wang and Baker, 2013; Gregory and others, 2014; Burr and others, 2018; Fourteau and others, 2019). For example, Srivastava and others (2010) calculated the elastic properties of snow from microtomography using a voxel-based finite element technique, and compared the results with several microstructural parameters, the best correlation being with ice volume fraction.

The results of microtomography are limited to small samples. In contrast, elastic waves can be used to obtain a continuous measure of elastic properties over large depth intervals. Gerling and others (2017) showed that elastic moduli derived from finite element analysis using the 3-D microstructure of snow reconstructed from microtomography agreed with elastic moduli derived from elastic wave velocity measurements for snow under laboratory conditions.

Snow and firn are porous media consisting of a porous ice frame and pore space containing air. The propagation of elastic waves in porous media such as snow and firn may be treated using Biot theory (Biot, 1956*a*, 1956*b*, Johnson, 1982*b*; Sidler, 2015). This requires, as input, the density and elastic properties of air and the porous ice frame. The objective of this paper is to provide a method for computing the elastic properties of the ice frame in

dry snow and firn using a physics-based approach that provides a consistent treatment of *P*- and *S*-velocities. The dynamic elastic properties are estimated using a modification of the differential effective medium scheme that accounts for the critical porosity ϕ_c (Nur and others, 1998) above which the bulk and shear moduli of the frame vanish.

Elastic wave velocities in snow and firn

Kohnen (1972) developed the following empirical relation between density and fast *P*-wave velocity based on measurements by Kohnen and Bentley (1973) near New Byrd Station in West Antarctica:

$$\rho(z) = \frac{\rho_{\text{ice}}}{1 + [(V_{P,\text{ice}} - V_P(z))/2.25\,\text{km s}^{-1}]^{1.22}}, \quad (1)$$

where $\rho(z)$ and $V_P(z)$ are the density and *P*-wave velocity at depth z, and ρ_{ice} and $V_{P,\text{ice}}$ are the density and *P*-wave velocity of ice.

Diez and others (2014) gave a similar empirical relation between density and *S*-wave velocity based on measurements at Kohnen Station, West Antarctica:

$$\rho(z) = \frac{\rho_{\text{ice}}}{1 + [(V_{S,\text{ice}} - V_S(z))/0.95\,\text{km s}^{-1}]^{1.17}}, \quad (2)$$

where $V_{S,\text{ice}}$ and $V_S(z)$ are the *S*-wave velocity of ice and at depth z, respectively. Relationships between density and velocity such as those in Eqns (1) and (2) have the potential to provide improved monitoring of the surface mass balance of glaciers and ice sheets using airborne or satellite altimetry by allowing the measured surface elevation to be corrected for compaction of snow.

Since snow and firn are porous media, their elastic wave velocities may be calculated using Biot theory (Biot, 1956*a*, 1956*b*, Johnson, 1982*b*; Sidler, 2015). Denoting angular frequency by ω, fluid viscosity by η and fluid density by ρ_f, the crossover from low to high frequency behavior occurs at a frequency ω_c at which the viscous skin depth, $\sqrt{2\eta/\rho_f\omega}$, is approximately equal to the pore radius, a, (Johnson, 1982*a*):

$$\omega_c = \frac{2\eta}{\rho_f a^2}. \quad (3)$$

Capelli and others (2016) list pore diameters in snow in the range 0.2–0.35 mm. For air with $\eta = 1.7 \times 10^{-5}$ Pa s, $\rho_f = 1.3$ kg m^{-3} (Sidler, 2015), Eqn (3) gives $\omega_c < 3$ kHz for this range of pore diameters.

At high frequency, this theory predicts that there is a fast compressional wave corresponding to the solid and fluid (air) moving in phase, a slow compressional wave corresponding to the solid and fluid moving out of phase, and one shear wave (Johnson, 1982*a*). At low frequency, the fast compressional and shear waves propagate, but the slow wave is described by the solution of a diffusion equation. These predictions are consistent with observations of *P*-wave velocities that increase with density and are faster than in air when sources in direct contact with the ice frame are used, but that are slower than in air when sources not in contact with the ice frame are used (Capelli and others, 2016).

In the high frequency limit of the theory, the velocities of the fast and slow compressional wave and shear wave are given in the Appendix following Johnson (1982*a*). To illustrate the nature of these predictions, the empirical expressions for the required properties of snow as a function of porosity used by Sidler (2015) based on prior information available in the literature are employed. Denoting porosity by ϕ, density and bulk modulus of the solid (ice) by ρ_s and K_s, and bulk and shear moduli of the ice frame by K_b and μ_b, the empirical relations used by Sidler (2015) are as follows:

$$K_b = K_s(1 - \phi)^{30.85/(7.76-\phi)}, \quad (4)$$

$$\mu_b = \frac{3K_b(1 - 2\nu_b)}{2(1 + \nu_b)}. \quad (5)$$

The following empirical relation for Poisson's ratio ν_b of the frame was used by Sidler (2015):

$$\nu_b = 0.38 - 0.36\phi. \quad (6)$$

Sidler (2015) assumes a value $K_s = 10$ GPa. Equation (5) then gives $\mu_s = 2.61$ GPa. An additional parameter required is a geometrical quantity $\tau > 1$ that increases as the tortuosity of the pore space increases. Sidler (2015) used the expression derived by Berryman (1980*a*) for the case of isolated spherical solid particles in the fluid:

$$\tau = \frac{1}{2}\left(1 + \frac{1}{\phi}\right). \quad (7)$$

Figure 1(a) shows the predictions of Biot theory in the high frequency limit obtained using these expressions.

Figure 1(b) shows a detailed view of the fast and slow *P*-wave velocities for density in the range 170–190 kg m^{-3}, where the curves appear to cross in the upper subplot. The dash-dotted and dotted curves in the lower figure show the predictions of the theory in the stiff frame limit (K_b, $\mu_b \gg K_f$, where K_f is the bulk modulus of the fluid). The fast and slow *P*-velocities in this limit are given by Johnson (1982*a*) as:

$$V_{P,\text{fast}}^{\text{stiff}} = \sqrt{\frac{K_b + 4\mu_b/3}{(1 - \phi)\rho_s + (1 - 1/\tau)\phi\rho_f}}, \quad (8)$$

$$V_{P,\text{slow}}^{\text{stiff}} = \frac{V_f}{\sqrt{\tau}}. \quad (9)$$

A comparison of the fast and slow compressional velocities in Figure 1(b) with these expressions shows that at low density, when the ice frame has low bulk and shear moduli, the slow compressional wave travels mainly on the ice frame, while the fast compressional travels mostly in the air phase. At higher density, the fast compressional wave travels mostly on the ice frame, while the slow compressional wave travels mostly in the air phase. Above a density of 190 kg m^{-3} the fast wave is accurately represented by the stiff frame limit given by Eqn (8) which is essentially independent of τ because of the low density of air in comparison with that of ice.

The most complete published datasets with measurements of density, fast *P*- and *S*-velocities are those of Smith (1965) and Yamada and others (1974). The red and blue points in Figure 1(a) show these data, which are seen to be in reasonable agreement with the velocity of the fast compressional wave predicted by Biot theory using the empirical relationships of Sidler (2015). The green stars show the data of Oura (1952), Ishida (1965), Marco and others (1998) and Gudra and Najwer (2011). The data of Yamada and others (1974), Oura (1952), Ishida (1965), Marco and others (1998) and Gudra and Najwer (2011) were taken from Capelli (2021). It is seen that as density increases the green stars fall below the velocity of the slow compressional

https://doi.org/10.1017/jog.2021.25 Published online by Cambridge University Press

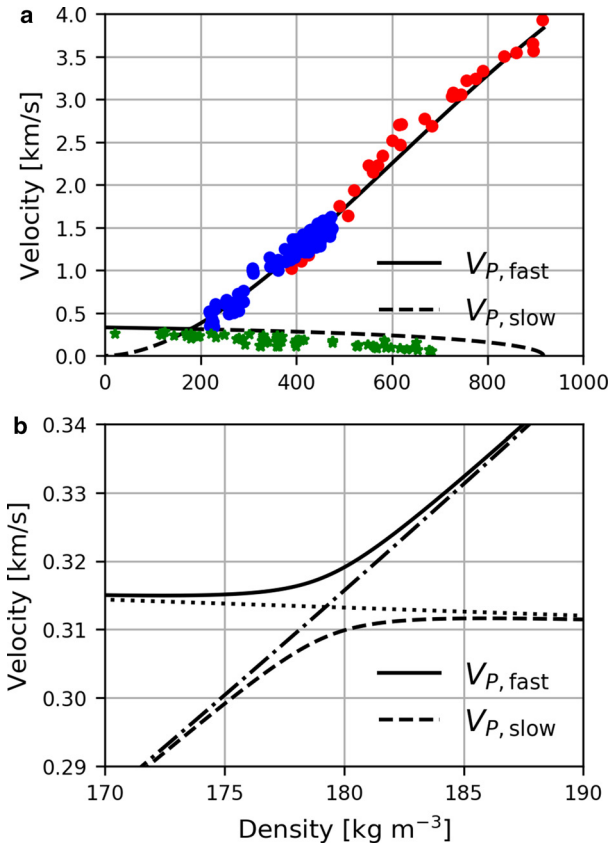

Fig. 1. Fast (full curve) and slow (dashed curve) *P*-wave velocities as a function of density as predicted by Biot theory. The circles in (a) show the data of Smith (1965) (red) and Yamada and others (1974) (blue), while the green stars show the data of Oura (1952), Ishida (1965), Marco and others (1998) and Gudra and Najwer (2011). Panel (b) shows a detailed view of the fast and slow *P*-wave velocities for density in the range 170–190 kg m^{-3}. The dash-dotted and dotted curves in (b) show the stiff frame predictions (K_b, $\mu_b \gg K_f$).

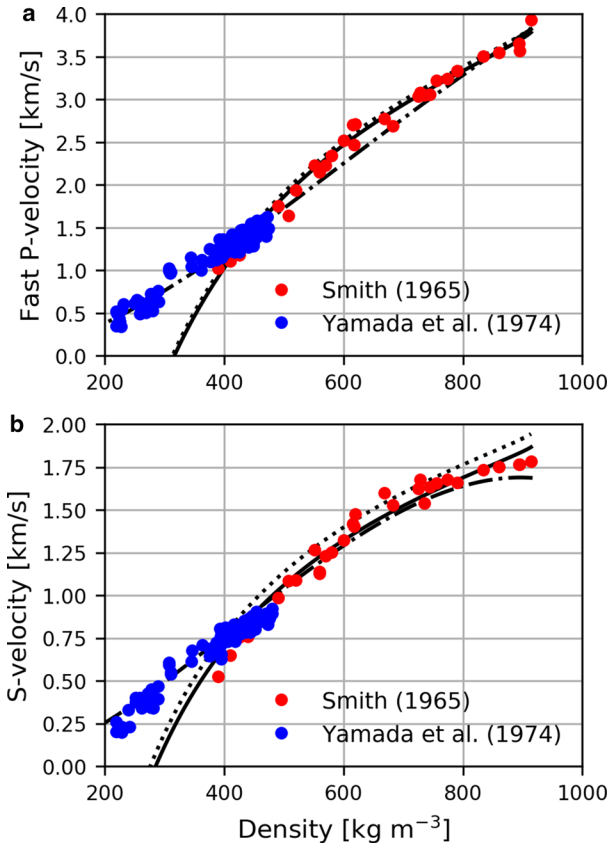

Fig. 2. Comparison between measurements of fast *P*-velocity (a) and *S*-velocity (b) in snow and firn measured by Smith (1965) (red points) and by Yamada and others (1974) (blue points) with fast *P*-velocity and *S*-velocity obtained using the empirical relations of Sidler (2015) (dash-dotted curves). The dotted curves show the predictions of Eqns (1) and (2) with *P*- and *S*-velocities $V_{P,\text{ice}}$ and $V_{S,\text{ice}}$ of ice computed using a density of ice of 915 kg m^{-3} given by Kohnen (1972) and bulk modulus K = 8.90 GPa and shear modulus μ = 3.46 GPa of isotropic polycrystalline ice calculated from the single crystal elastic stiffnesses of Gammon and others (1983). The full curves show the predictions of Eqns (1) and (2) using a reduced shear modulus μ = 3.20 GPa for isotropic polycrystalline ice.

predicted by Biot theory using the parameters of Sidler (2015). This suggests that τ is greater than that predicted by Eqn (7), and that the tortuosity of the pore space in snow and firn is greater than that assumed in deriving this equation. This is consistent with the observations of Schwander and others (1988) who found high tortuosity factors for firn samples, as compared to a sphere pack, indicating the existence of dead-end channels and/or relatively narrow passages in the pore channels. The absence of measurements of the slow wave at high density probably results from the high tortuosity of the pore space at high density.

Figure 2 compares the predictions of the empirical relations given by Eqns (1) and (2) with the measurements of Smith (1965) and Yamada and others (1974). The dotted curves correspond to *P*- and *S*-velocities $V_{P,\text{ice}}$ and $V_{S,\text{ice}}$ of ice estimated using density of ice of 915 kg m^{-3} given by Kohnen (1972) and bulk modulus K_s = 8.90 GPa and shear modulus μ_s = 3.46 GPa of isotropic polycrystalline ice calculated from the single crystal elastic stiffnesses of Gammon and others (1983) listed in Table 1 using the Hill (1952) average of the Voigt (1910) and Reuss (1929) bounds. The elastic moduli of Gammon and others (1983) were chosen for this comparison since these are the most recent measurements of the single crystal elastic stiffness coefficients of ice in Table 1. Also shown by the dash-dotted curves in Figure 2 are the predictions of Biot theory using the empirical relations of Sidler (2015) listed above.

It is seen in Figure 2(a) that Eqn (1) with bulk modulus of isotropic polycrystalline ice obtained from the single crystal elastic stiffnesses of Gammon and others (1983) agrees best with the measurements of Smith (1965), while the fast *P*-velocity obtained using the empirical relations of Sidler (2015) agree best with the measurements of Yamada and others (1974). Figure 2(b) shows that Eqn (2) with shear modulus μ_s = 3.46 GPa of isotropic polycrystalline ice obtained from the single crystal elastic stiffnesses of Gammon and others (1983) overestimates the measured *S*-velocities, while Biot theory using the empirical relations of Sidler (2015) underestimates the *S*-velocities at high density. The shear modulus at zero porosity calculated from Eqns (4) and (5) used by Sidler (2015) is μ_s = 2.61 GPa, which is significantly less than any of the shear moduli for isotropic polycrystalline ice given in Table 1. The full curve in Figure 2(b) shows the prediction of Eqn (2) for a shear modulus μ_s = 3.20 GPa. At high density, this is seen to give a much better prediction than that calculated from the data of Gammon and others (1983) and is the value used in the rest of this paper.

Poisson's ratio ν may be calculated from V_P and V_S as follows:

$$\nu = \frac{V_P^2 - 2V_S^2}{2(V_P^2 - 2V_S^2)}. \tag{10}$$

Figure 3 compares Poisson's ratio ν as a function of fast compressional velocity computed by combining Eqns (1) and (2) using bulk modulus K_s = 8.90 GPa and shear modulus μ_s = 3.46 GPa of isotropic polycrystalline ice calculated from the single crystal elastic stiffnesses of Gammon and others (1983) (dotted

https://doi.org/10.1017/jog.2021.25 Published online by Cambridge University Press

Table 1. Single crystal elastic stiffnesses (GPa) of ice measured by Jona and Scherrer (1952), Green and Mackinnon (1956), Bass and others (1957), Brockamp and Querfurth (1964), Dantl (1968), Bennett (1968) and Gammon and others (1983) compiled by Gusmeroli and others (2012) together with computed Voigt (V), Reuss (R) and Hill (H) estimates K_V, K_R, K_H, μ_V, μ_R, μ_H, M_V, M_R, M_H, ν_V, ν_R and ν_H of the bulk K, shear μ and compressional $M = K + 4\mu/3$ moduli and Poisson's ratio of an isotropic polycrystalline aggregate of ice crystals

	Jona and Scherrer	Green and Mackinnon	Bass and others	Brockamp and Querfurth	Dantl	Bennett	Gammon and others
C_{11}	13.85	13.33	13.3	13.63	13.2	14.06	13.94
C_{33}	14.99	14.28	14.2	14.85	14.42	15.24	15.0
C_{55}	3.19	3.26	3.06	3.04	2.89	3.06	3.01
C_{66}	3.39	3.65	3.5	3.47	3.26	3.46	3.43
C_{12}	7.07	6.03	6.3	6.69	6.69	7.15	7.08
C_{13}	5.81	5.08	4.6	5.15	5.84	5.88	5.76
K_V	8.89	8.15	7.98	8.45	8.62	9.02	8.90
K_H	8.89	8.15	7.98	8.45	8.62	9.02	8.90
K_R	8.89	8.15	7.97	8.45	8.61	9.02	8.90
μ_V	3.55	3.68	3.61	3.58	3.31	3.55	3.51
μ_H	3.52	3.66	3.56	3.53	3.27	3.50	3.46
μ_R	3.49	3.63	3.50	3.48	3.24	3.46	3.42
M_V	13.63	13.06	12.79	13.23	13.02	13.75	13.58
M_H	13.59	13.02	12.72	13.16	12.98	13.69	13.52
M_R	13.54	12.98	12.64	13.09	12.94	13.63	13.46
ν_V	0.324	0.304	0.303	0.314	0.330	0.326	0.326
ν_H	0.325	0.305	0.306	0.317	0.331	0.328	0.328
ν_R	0.327	0.306	0.308	0.319	0.333	0.330	0.330

curve) and by using the empirical relation of Sidler (2015) given by Eqn (6) (dash-dotted curve). The full curve shows the predictions of Eqns (1) and (2) using a reduced shear modulus $\mu = 3.20$ GPa for isotropic polycrystalline ice. It is seen that Eqns (1) and (2) may lead to very small and even negative values of Poisson's ratio at low density, while $\nu > 0$ for isotropic materials. The scatter in Poisson's ratio in Figure 3 is much greater than that in the velocities in Figure 2 as is expected from Eqn (10). As an example, Christensen (1996) notes that an error of over 9% in Poisson's ratio can result from errors of 2% in both V_P and V_S. For this reason, Poisson's ratio calculated from the measurements of Yamada and others (1974) are not shown in Figure 3, since V_P and V_S for this dataset were digitized from the plots in Yamada and others (1974) so that the errors in V_P and V_S are presumably greater than in the original measurements.

Although the empirical fits of Sidler (2015), Kohnen (1972) and Diez and others (2014) give a reasonable description of the data over the porosity range for which they were calibrated, they do not provide much insight into the underlying mechanisms for such relations. For example, it is not clear how to modify such relations to investigate the role of anisotropy, pore shape, etc. In contrast, a physics-based approach allows variations in anisotropy, pore shape, etc. to be investigated. In the following section, one possible physics-based approach is introduced and compared with the measurements of Smith (1965) and Yamada and others (1974) plotted in Figure 2.

Theoretical approach

To estimate the bulk and shear moduli of the porous ice frame, the differential effective medium scheme will be used. This has been reviewed, for example, by Norris (1985) and Zimmerman (1990), and has been used widely to estimate the elastic properties of porous media with interconnected pore space such as porous sandstones (e.g. Zimmerman, 1990; Berge and others, 1993; Berryman, 2004; Li and Zhang, 2010).

Consider a two phase medium with bulk and shear moduli of phase i =1, 2 denoted by K_i and μ_i. In the differential effective

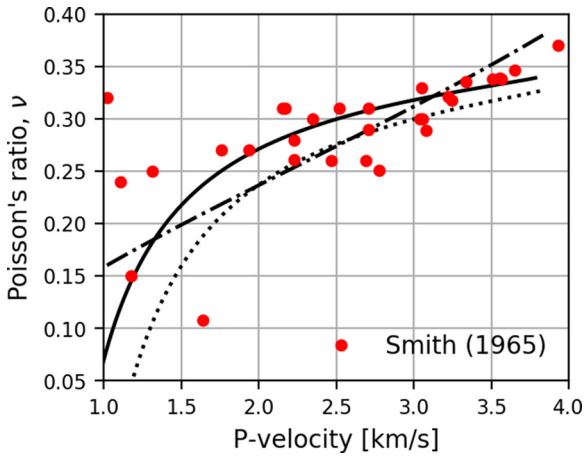

Fig. 3. Poisson's ratio calculated by combining Eqns (1) and (2) and from the empirical relation of Sidler given by Eqn (6) (dash-dotted curve) compared with that calculated from the measurements of Smith (1965) (red points). The dotted curves show the predictions of Eqns (1) and (2) with P- and S-velocities $V_{P,\mathrm{ice}}$ and $V_{S,\mathrm{ice}}$ of ice computed using a density of ice of 915 kg m^{-3} given by Kohnen (1972) and bulk modulus $K = 8.90$ GPa and shear modulus $\mu = 3.46$ GPa of isotropic polycrystalline ice calculated from the single crystal elastic stiffnesses of Gammon and others (1983). The full curve shows the prediction of Eqn (2) using a reduced shear modulus $\mu = 3.20$ GPa of isotropic polycrystalline ice.

medium scheme the effective elastic properties of the medium are modeled by adding inclusions of one phase into the effective medium in a stepwise fashion. The effective medium begins as phase 1, but is altered at each step as an additional increment of phase 2 is added. Assuming that the two phases and the orientation distribution of inclusions are isotropic leads to two coupled differential equations for the effective bulk and shear moduli K_{eff} and μ_{eff} (Berryman, 1992):

$$(1-y)\frac{\mathrm{d}}{\mathrm{d}y}K_{\mathrm{eff}}(y) = (K_2 - K_{\mathrm{eff}})P(y), \tag{11}$$

$$(1-y)\frac{\mathrm{d}}{\mathrm{d}y}\mu_{\mathrm{eff}}(y) = (\mu_2 - \mu_{\mathrm{eff}})Q(y), \tag{12}$$

with initial conditions $K_{\mathrm{eff}}(0) = K_1$, $\mu_{\mathrm{eff}}(0) = \mu_1$. The quantity y is the volume fraction of phase 2. The quantities P and Q depend on the shape of the inclusions and, for ellipsoidal inclusions, have been given by Berryman (1980*b*).

Application to dry snow and firn

The elastic properties of ice may be estimated using the Hill (1952) average of the Voigt (1910) and Reuss (1929) bounds for the bulk and shear moduli of isotropic polycrystalline ice. Ice that occurs naturally on Earth has a hexagonal crystallographic symmetry. The elastic stiffness tensor of a crystal with hexagonal symmetry is transversely isotropic with the axis of rotational symmetry (*c*-axis) perpendicular to the basal plane. Taking the x_3 axis to lie along the axis of rotational symmetry, the non-vanishing elastic stiffness coefficients are $C_{11} = C_{22}$, C_{33}, $C_{44} = C_{55}$, C_{66}, $C_{12} = C_{11} - 2C_{66}$ and $C_{13} = C_{23}$ in conventional two-index notation (Voigt, 1910; Nye, 1985). Table I lists measured single crystal elastic constants for ice compiled by Gusmeroli and others (2012), together with the computed Voigt (V), Reuss (R) and Hill (H) estimates K_V, K_R, K_H, μ_V, μ_R, μ_H, M_V, M_R, M_H, ν_V, ν_R and ν_H of the bulk K, shear μ and compressional $M = K + 4\mu/3$ moduli and Poisson's ratio ν of an isotropic polycrystalline aggregate of ice crystals. For a given set of elastic stiffnesses, the bulk modulus

https://doi.org/10.1017/jog.2021.25 Published online by Cambridge University Press

is seen to be tightly bound by the Voigt and Reuss averages, but the shear modulus is less constrained due to the greater shear wave anisotropy of single crystals of ice. Figure 2 shows that at high density the bulk modulus $K_s = 8.90$ GPa of isotropic polycrystalline ice obtained from the single crystal elastic stiffnesses of Gammon and others (1983) listed in Table I using the Hill (1952) average of the Voigt (1910) and Reuss (1929) bounds gives a good description of the *P*-wave data. However, the shear modulus $\mu_s = 3.46$ GPa calculated from the single crystal elastic stiffnesses of Gammon and others (1983) is too high and a reduced value $\mu_s = 3.20$ GPa gives a better description of the shear wave data at high density shown in the lower subplot of Figure 2. For this reason, we use the values $K_s = 8.90$ GPa, $\mu_s = 3.20$ GPa below.

Figure 4 shows the bulk and shear moduli of the ice frame in snow and firn as a function of porosity obtained using the differential effective medium scheme (Norris, 1985; Zimmerman, 1990). The pores are modeled as oblate spheroids. An oblate spheroid is an ellipsoid obtained by rotating an ellipse about its minor axis, with equatorial dimension a greater than the polar dimension c. The curves in Figure 4 are plotted for pore aspect ratios of 0.1, 0.2, 0.4 and 1. Also shown are the measurements of Smith (1965) and Yamada and others (1974). Porosity is calculated from measured density as follows:

$$\phi = \frac{\rho_s - \rho}{\rho_s - \rho_f}. \tag{13}$$

Here, ρ is the density of snow or firn, ρ_s is the density of ice and ρ_f is the density of the fluid in the pore space, assumed to be air. The density of ice is assumed to be $\rho_s = 915$ kg m^{-3} given by Kohnen (1972). It is seen that at low porosity the predicted bulk and shear moduli are consistent with the pores having a spherical shape (aspect ratio = 1), as observed also in glacial ice. As porosity increases, however, the measurements fall below the curve corresponding to an aspect ratio of 1. This may indicate that the pores have a lower aspect ratio at higher porosity. However, the elastic moduli only become zero in the limit $\phi \to 1$ in this scheme, while the elastic moduli are expected to vanish at a critical porosity $\phi_c < 1$, estimated by Sidler (2015) to be $\phi_c = 0.8$ for snow. Also, pores in firn close and trap interstitial air in airtight bubbles as porosity reduces below a value of ~0.1 referred to as pore close-off (Stauffer and others, 1985; Schaller and others, 2017; Fourteau and others, 2020). Above this value of porosity the connectivity of the pore space is important.

Although widely used, the differential medium scheme has the disadvantage that the elastic moduli of a porous medium are predicted to vanish only in the limit $\phi \to 1$. For most porous media, however, the elastic moduli only become non-zero as porosity drops below a critical value ϕ_c, referred to as the critical porosity (Nur and others, 1998). To account for this, Mukerji and others (1995) proposed a modification of the differential effective medium scheme in which the properties of the inclusions are taken as those of the porous medium at the critical porosity. The pore space within the inclusions is therefore interconnected, and the pores are not assumed to have any particular shape. Sidler (2015) estimates ϕ_c as 0.8 for snow, while the porosity of fresh, uncompacted snow is typically of order 0.9–0.95 (National Snow and Ice Data Center, 2021). In the following, the value $\phi_c = 0.9$ is used for the purpose of illustration. The approach is not limited to this value, however, and different values may be used as required.

Figure 5 shows the results of a modified differential effective medium scheme that takes into account the vanishing of the elastic moduli at a critical porosity $\phi_c = 0.9$ and the interconnectivity of the pore space above the pore close-off porosity, assumed to be

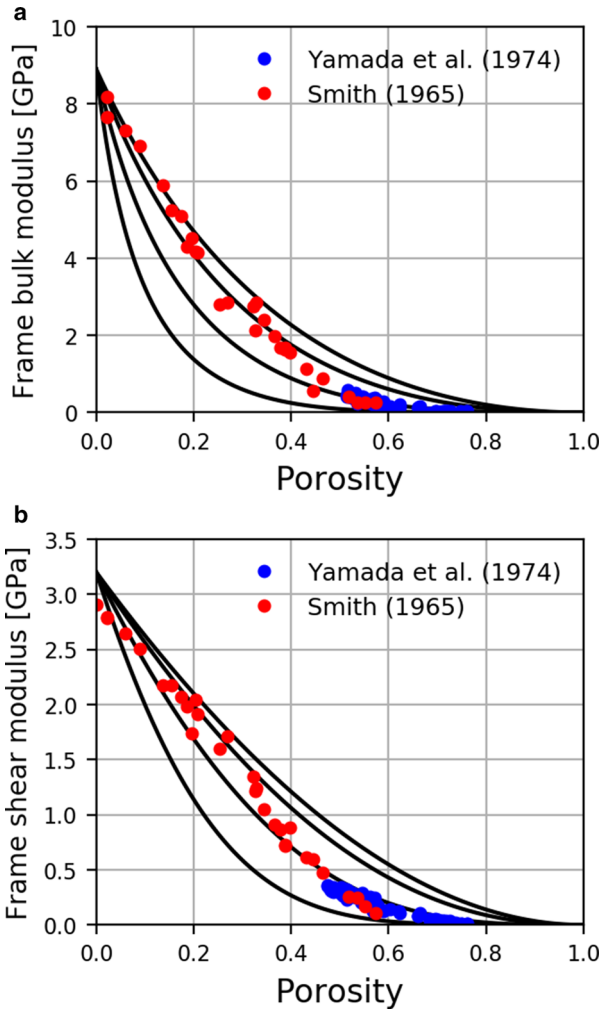

Fig. 4. (a) Bulk and (b) shear moduli (full curves) of the ice frame in dry snow and firn obtained using the differential effective medium scheme (Norris, 1985; Zimmerman, 1990) for pore aspect ratios of 0.1 (lower curve), 0.2, 0.4 and 1 (upper curve). The symbols show the measurements of Smith (1965) (red points) and Yamada and others (1974) (blue points).

0.1. For porosities <0.1 the original differential medium scheme is used in which discrete pores are added to the effective medium. Above a porosity of 0.1, however, phase 1 is taken to have bulk and shear moduli of the medium in Figure 4 at a porosity of 0.1 and phase 2 is taken to have the properties of the medium at critical porosity $\phi_c = 0.9$. Comparison of the predicted bulk and shear moduli with those calculated from the *P*- and *S*-velocity measurements of Smith (1965) and Yamada and others (1974) plotted in figure 5 shows that the modified differential effective medium scheme gives a good description of the data. The elastic moduli are found to vanish for porosity greater than the critical porosity $\phi_c = 0.9$ without the need to assume small pore aspect ratios at high porosity as in Figure 4.

Discussion

The previous section showed that the elastic moduli predicted using the modified differential effective medium scheme agree well with those deduced from the fast *P*- and *S*-velocity measurements of Smith (1965) and Yamada and others (1974). However, the shear modulus of ice in snow used is lower than values computed from the single crystal elastic stiffnesses of ice shown in Table I. This may indicate that the bond between ice particles is not perfect. To illustrate this, consider Figure 6, which shows a

https://doi.org/10.1017/jog.2021.25 Published online by Cambridge University Press

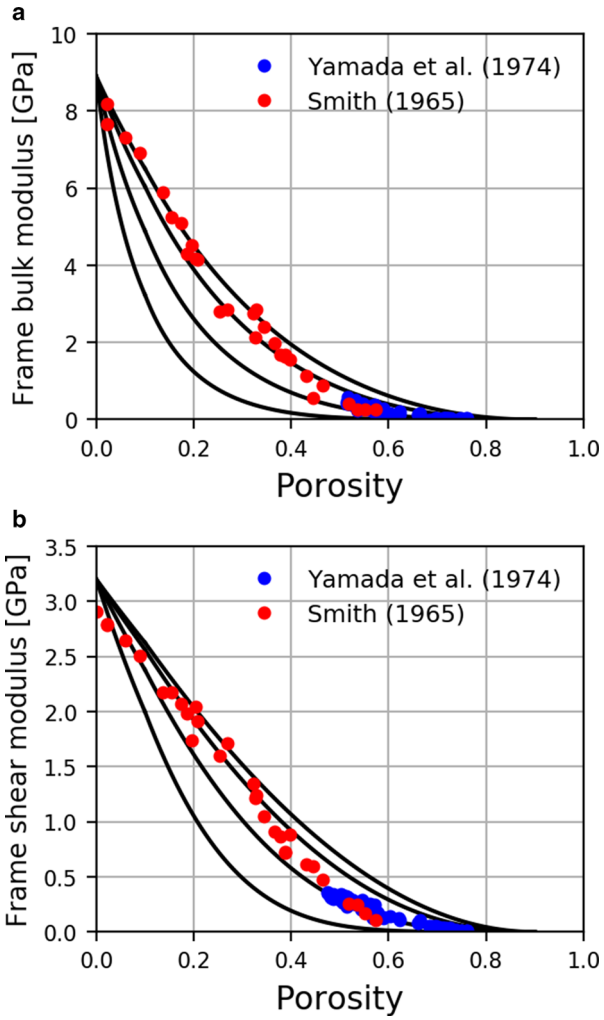

Fig. 5. (a) Bulk and (b) shear moduli (full curves) of the ice frame in dry snow and firn obtained using the modified differential effective medium scheme described in this paper assuming a critical porosity $\phi_c = 0.9$ for inclusion aspect ratios of 0.1 (lower curve), 0.2, 0.4 and 1 (upper curve). The symbols show the measurements of Smith (1965) (red points) and Yamada and others (1974) (blue points).

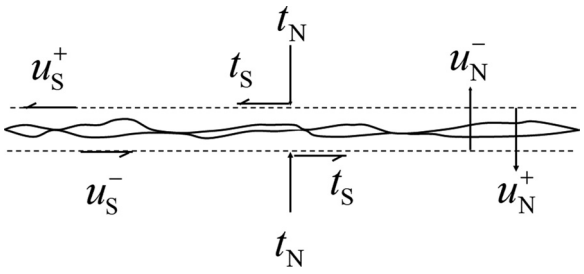

Fig. 6. Schematic representation of part of a bond between two ice particles in snow or firn modeled as a locally flat imperfectly bonded interface. The normal and shear displacements of the upper face of the interface are denoted by u_N^+ and u_S^+, whereas those of the lower face are denoted by u_N^- and u_S^-. The normal and shear tractions are denoted by t_N and t_S, respectively.

schematic representation of the interface between two ice particles in snow or firn. The bond between ice particles is treated as an imperfectly bonded interface across which the traction vector with Cartesian components t_i, $i = 1, 2, 3$ is continuous but the displacement vector with Cartesian components u_i may be discontinuous. Following Schoenberg (1980) and Kachanov (1992) we assume that the discontinuity in displacement $[u_i] \equiv u_i^+ - u_i^-$ between opposing faces of an interface is linear in the traction, so that

$$[u_i] = B_{ij} t_j. \tag{14}$$

Here, B_{ij} are components of the second-rank compliance tensor characterizing the mechanical properties of the interface, and the Einstein summation convention is adopted in which a sum over repeated indices is implied.

The contribution of the interfaces to the effective elastic properties may be written (Kachanov, 1992; Sayers and Kachanov, 1995) in terms of a second- and fourth-rank tensor α_{ij} and β_{ijkl} defined by Kachanov (1992):

$$\alpha_{ij} = \frac{1}{V} \sum_{r=1}^{N} B_S^{(r)} n_i^{(r)} n_j^{(r)} A^{(r)}, \tag{15}$$

$$\beta_{ijkl} = \frac{1}{V} \sum_{r=1}^{N} (B_N^{(r)} - B_S^{(r)}) n_i^{(r)} n_j^{(r)} n_k^{(r)} n_l^{(r)} A^{(r)}. \tag{16}$$

The terms $B_N^{(r)}$ and $B_S^{(r)}$ are the effective normal and shear compliance of the rth interface in volume V, $n_i^{(r)}$ is the ith component of the normal to the rth interface and $A^{(r)}$ is the area of the rth interface (Kachanov, 1992; Sayers and Kachanov, 1995).

Assuming that snow and firn are isotropic, the non-vanishing components of α_{ij} and β_{ijkl} are:

$$\alpha_{11} = \alpha_{22} = \alpha_{33} \equiv \alpha, \tag{17}$$

$$\beta_{1111} = \beta_{2222} = \beta_{3333} \equiv \beta, \tag{18}$$

$$\beta_{1122} = \beta_{1133} = \beta_{2233} = \beta_{1212} = \beta_{1313} = \beta_{2323} = \beta/3. \tag{19}$$

It then follows (Sayers and Han, 2002; Sayers, 2018) that the bulk and shear moduli of the medium in the presence of imperfect bonds between the ice particles are:

$$K = \frac{K_0}{1 + 3K_0\alpha(1 + 5\beta/(3\alpha))}, \tag{20}$$

$$\mu = \frac{\mu_0}{1 + 2\mu_0\alpha(1 + 2\beta/(3\alpha))}, \tag{21}$$

where K_0 and μ_0 are the bulk and shear moduli that would result if the bonds between ice particles were perfect. It follows from Eqns (15) and (16) that $5\beta/(3\alpha) = (B_N/B_S) - 1$, assuming an isotropic distribution of normal vectors n_i. Equations (20) and (21) then give:

$$K = \frac{K_0}{1 + 3K_0\alpha B_N/B_S}, \tag{22}$$

$$\mu = \frac{\mu_0}{1 + 2\mu_0\alpha(3 + 2B_N/B_S)/5}. \tag{23}$$

It is seen that if B_N/B_S is small the bulk modulus K is relatively unaffected by the presence of imperfect bonding between ice particles, while the shear modulus μ is reduced significantly. Thus the reduced value of the shear modulus of ice required to obtain

https://doi.org/10.1017/jog.2021.25 Published online by Cambridge University Press

agreement with the shear modulus of snow and firn calculated from the *P*- and *S*-velocity measurements of Smith (1965) and Yamada and others (1974) in the preceding sections may indicate that the bonds between ice particles in snow and firn are more deformable under shear than under compression.

Although the reduced shear modulus $\mu_s = 3.20$ GPa used in the previous section gave good overall agreement with the measured elastic moduli shown in Figure 5, the shear modulus calculated from the measured *S*-wave velocities of Smith (1965) for low porosity are lower than this value. This may indicate that the *c*-axes of ice crystals in snow and firn investigated by Smith (1965) become partially aligned as porosity decreases. In support of this it is seen in Table I that the shear modulus C_{55} corresponding both to *S*-wave propagation along the *c*-axis, and to *S*-wave propagation perpendicular to the *c*-axis with polarization along the *c*-axis, is significantly smaller than that given by the Hill average μ_H. Since the elastic stiffness C_{33} corresponding to *P*-wave propagation along the *c*-axis is significantly higher than the Hill average M_H, while the elastic stiffness C_{11} corresponding to *P*-wave propagation perpendicular to the *c*-axis is reasonably close to M_H a comparison with Figures 4 and 5 suggests that the direction of propagation would need to be approximately perpendicular to the *c*-axes of the ice crystals for anisotropy to explain the reduced shear modulus at low porosity. Unfortunately, the direction of propagation is not given by Smith (1965), so that this hypothesis cannot be checked. Finally, it should be noted that the five lowest porosity samples ($\rho > 800$ kg m^{-3}) studied by Smith (1965) were obtained by thermal drilling, while those with density ($\rho <$ 800 kg m^{-3}) were obtained using a 3-in diameter snow auger. If partial melting of the bonds between ice particles occurred during thermal drilling this might explain these low values of shear modulus following the discussion above. Alternatively, if thermal drilling led to the presence of liquid water in the pore space then the porosity calculated from density would be higher than shown in Figures 4 and 5 leading to the low porosity points in these figures being moved to higher porosity, as can be seen from Eqn (13).

Conclusion

Elastic wave velocity measurements provide a non-destructive method for estimating the mechanical properties, elastic wave velocities and density of snow and firn. Mechanical properties are needed for applications such as construction on snow, snow removal, vehicle mobility and avalanche release and control (Salm, 1982). The elastic moduli of snow and firn are required for the interpretation of seismic measurements, which have been used to monitor and locate avalanches (Suriñach and others, 2005; Van Herwijnen and Schweizer, 2011; Lacroix and others, 2012). Estimates of the variation of density with depth in snow deposited on glaciers and ice sheets enable improved monitoring of the surface mass balance of glaciers and ice sheets using airborne or satellite altimetry by allowing the measured surface elevation over time to be corrected for compaction of snow.

The elastic moduli of dry snow and firn are modeled using a modified differential effective medium scheme that accounts for the critical porosity above which the bulk and shear moduli of the frame vanish. The most complete datasets with measurements of density, fast *P*- and *S*-velocities are those of Smith (1965) and Yamada and others (1974). The expressions for the elastic properties of snow and firn as a function of porosity are compared, therefore, with these measurements. Comparison of the predicted bulk and shear moduli with those calculated from the *P*- and *S*-velocity measurements of Smith (1965) and Yamada and others (1974) shows that the modified differential effective medium scheme gives a good description of the data. This method is consistent with the expected zero moduli for porosity greater than a critical porosity ϕ_c, assumed in this paper to take the value 0.9, and does not require an assumption of small pore aspect ratios at high porosity as needed with the original differential effective medium scheme. The results suggest that the shear modulus of ice in snow and firn is lower than that computed from single crystal elastic stiffnesses of ice. This may indicate that the bonds between snow particles are more deformable under shear than under compression. A partial alignment of ice crystals also may contribute.

It should be noted that the pore space in snow and firn is assumed, in this paper, to be air-filled, and no correction for the presence of melt water was performed since information on the presence or absence of melt water in the samples for which measurements were made was not available. Melting and refreezing would lead to a stiffening of the ice frame and an increase in the elastic moduli, and this would need to be corrected for if it occurs.

The model of elastic moduli of snow and firn as a function of porosity reported here is simple and compact, and does not require the use of empirical fits to the data. Owing to its simplicity, it is anticipated that this model may be useful in a variety of potential applications such as construction on snow, interpretation of seismic measurements to monitor and locate avalanches, and estimation of density within compacting snow deposited on glaciers and ice sheets.

Acknowledgements. I thank Achille Capelli for providing the data in Capelli (2021), and the reviewers and Scientific Editor for many useful comments that lead to a significantly improved manuscript.

References

Bass R, Rossberg D and Ziegler G (1957) Die elastischen konstanten des Eises. *Zeitschrift für Physik* **149**(2), 199–203.

Bennett HF (1968) An Investigation into Velocity Anisotropy through Measurements of Ultrasonic Wave Velocities in Snow and Ice Cores from Greenland and Antarctica (Ph.D. thesis). University of Wisconsin.

Berge PA, Berryman JG and Bonner BP (1993) Influence of microstructure on rock elastic properties. *Geophysical Research Letters* **20**(23), 2619–2622.

Berryman JG (1980*a*) Confirmation of Biot's theory. *Applied Physics Letters* **37**(4), 382–384.

Berryman JG (1980*b*) Long-wavelength propagation in composite elastic media II. Ellipsoidal inclusions. *The Journal of the Acoustical Society of America* **68**(6), 1820–1831.

Berryman JG (1992) Single-scattering approximations for coefficients in Biot's equations of poroelasticity. *The Journal of the Acoustical Society of America* **91**(2), 551–571.

Berryman JG (2004) Modeling high-frequency acoustic velocities in patchy and partially saturated porous rock using differential effective medium theory. *International Journal for Multiscale Computational Engineering* **2**(1), 115–131.

Biot M (1956*a*) Theory of elastic waves in a fluid-saturated porous solid. 1. Low frequency range. *The Journal of the Acoustical Society of America* **28**, 168–178.

Biot MA (1956*b*) Theory of propagation of elastic waves in a fluid-saturated porous solid. II. Higher frequency range. *The Journal of the Acoustical Society of America* **28**(2), 179–191.

Brockamp B and Querfurth H (1964) Untersuchungen über die Elastizitätskonstanten von See-und Kunsteis. *Polarforschung* **34**(1/2)253–262.

Burr A, and 5 others (2018) Pore morphology of polar firn around closure revealed by X-ray tomography. *The Cryosphere* **12**, 2481–2500.

Capelli A (2021) Literature data of sound speed in snow. EnviDat. Available at https://doi.org/10.16904/envidat.204. doi: 10.16904/envidat.204.

Capelli A, Kapil JC, Reiweger I, Or D and Schweizer J (2016) Speed and attenuation of acoustic waves in snow: laboratory experiments and modeling with Biot's theory. *Cold Regions Science and Technology* **125**, 1–11.

Christensen NI (1996) Poisson's ratio and crustal seismology. *Journal of Geophysical Research: Solid Earth* **101**(B2), 3139–3156.

Cuffey KM and Paterson WSB (2010) *The Physics of Glaciers*. Amsterdam: Elsevier.

Dantl G (1968) Die elastischen moduln von eis-einkristallen. *Physik der kondensierten Materie* **7**(5), 390–397.

Diez A and 7 others (2014) Influence of ice crystal anisotropy on seismic velocity analysis. *Annals of Glaciology* **55**(67), 97–106.

Fourteau K and 11 others (2019) Multi-tracer study of gas trapping in an East Antarctic ice core. *The Cryosphere* **13**(12), 3383-3403.

Fourteau K and 6 others (2020) Historical porosity data in polar firn. *Earth System Science Data* **12**(2), 1171–1177.

Gammon PH, Kiefte H, Clouter MJ and Denner WW (1983) Elastic constants of artificial and natural ice samples by Brillouin spectroscopy. *Journal of Glaciology* **29**(103), 433–460.

Gerling B, Löwe H and van Herwijnen A (2017) Measuring the elastic modulus of snow. *Geophysical Research Letters* **44**(21), 11–088.

Green RE and Mackinnon L (1956) Determination of the elastic constants of ice single crystals by an ultrasonic pulse method. *The Journal of the Acoustical Society of America* **28**(6), 1292–1292.

Gregory SA, Albert MR and Baker I (2014) Impact of physical properties and accumulation rate on pore close-off in layered firn. *The Cryosphere* **8**(1), 91–91.

Gudra T and Najwer L (2011) Ultrasonic investigation of snow and ice parameters. *Acta Physica Polonica A* **120**(4), 625–629.

Gusmeroli A, Pettit EC, Kennedy JH and Ritz C (2012) The crystal fabric of ice from full-waveform borehole sonic logging. *Journal of Geophysical Research: Earth Surface* **117**, F03021.

Hill R (1952) The elastic behaviour of a crystalline aggregate. *Proceedings of the Physical Society London, Series A* **65**(5), 349–354.

Ishida T (1965) Acoustic properties of snow. *Contributions from the Institute of Low Temperature Science* **20**, 23–63.

Johnson DL (1982*a*) Elastodynamics of porous media. In Burridge R, Childress S and Papanicolaou G eds. *Macroscopic Properties of Disordered Media*. Berlin, Heidelberg: Springer, pp. 97–110.

Johnson J (1982*b*) On the application of Biot's theory to acoustic wave propagation in snow. *Cold Regions Science and Technology* **6**(1), 49–60.

Jona VF and Scherrer P (1952) Die elastischen Konstanten von Eis-Einkristallen. *Helvetica Physica Acta* **25**(1-2), 33–54.

Kachanov M (1992) Effective elastic properties of cracked solids: critical review of some basic concepts. *Applied Mechanics Reviews* **45**(8), 304–335.

Kaempfer TU and Schneebeli M (2007) Observation of isothermal metamorphism of new snow and interpretation as a sintering process. *Journal of Geophysical Research* **112**, D24101.

Köchle B and Schneebeli M (2014) Three-dimensional microstructure and numerical calculation of elastic properties of alpine snow with a focus on weak layers. *Journal of Glaciology* **60**(222), 705–713.

Kohnen H (1972) Über die Beziehung zwischen seismischen Geschwindigkeiten und der Dichte in Firn und Eis. *Zeitschrift für Physik* **38**, 925–935.

Kohnen H and Bentley CR (1973) Seismoglaziologische Untersuchungen nahe Byrd Station, Antarktis. *Archiv für Meteorologie, Geophysik und Bioklimatologie, Serie A* **22**(2-3), 311–324.

Lacroix P and 6 others (2012) Monitoring of snow avalanches using a seismic array: location, speed estimation, and relationships to meteorological variables. *Journal of Geophysical Research: Earth Surface* **117**, F01034, 1–15.

Li H and Zhang J (2010) Modulus ratio of dry rock based on differential effective-medium theory. *Geophysics* **75**(2), N43–N50.

Marco O, Buser O, Villemain P, Touvier F and Revol P (1998) Acoustic impedance measurement of snow density. *Annals of Glaciology* **26**, 92–96.

Mellor M (1974) A review of basic snow mechanics. US Army Cold Regions Research and Engineering Laboratory.

Mukerji T, Berryman J, Mavko G and Berge P (1995) Differential effective medium modeling of rock elastic moduli with critical porosity constraints. *Geophysical Research Letters* **22**(5), 555–558.

National Snow and Ice Data Center (2021) Snow characteristics. Available at https://nsidc.org/cryosphere/snow/science/characteristics.html.

Norris AN (1985) A differential scheme for the effective moduli of composites. *Mechanics of Materials* **4**(1), 1–16.

Nur A, Mavko G, Dvorkin J and Galmudi D (1998) Critical porosity: a key to relating physical properties to porosity in rocks. *The Leading Edge* **17**(3), 357–362.

Nye JF(1985) *Physical Properties of Crystals: Their Representation by Tensors and Matrices*. Oxfor: Oxford University Press.

Ohser J, Redenbach C and Schladitz K (2009) Mesh free estimation of the structure model index. *Image Analysis & Stereology* **28**(3), 179–185.

Oura H (1952) Sound velocity in the snow cover. *Low Temperature Science. Series A, Physical Sciences* **9**, 171–178.

Pieritz RA, Brzoska JB, Flin F, Lesaffre B and Coléou C (2004) From snow X-ray microtomograph raw volume data to micromechanics modeling: first results. *Annals of glaciology* **38**, 52–58.

Reuss A (1929) Berechnung der fließgrenze von mischkristallen auf grund der plastizitätsbedingung für einkristalle. *ZAMM-Journal of Applied Mathematics and Mechanics/Zeitschrift für Angewandte Mathematik und Mechanik* **9**(1), 49–58.

Salm B (1982) Mechanical properties of snow. *Reviews of Geophysics* **20**(1), 1–19.

Sayers CM (2018) Increasing contribution of grain boundary compliance to polycrystalline ice elasticity as temperature increases. *Journal of Glaciology* **64**(246), 669–674.

Sayers CM and Han DH (2002) The effect of pore fluid on the stress-dependent elastic wave velocities in sandstones. In *SEG Technical Program Expanded Abstracts 2002*. Society of Exploration Geophysicists, pp. 1842–1845.

Sayers CM and Kachanov M (1995) Microcrack-induced elastic wave anisotropy of brittle rocks. *Journal of Geophysical Research: Solid Earth* **100**(B3), 4149–4156.

Schaller CF, Freitag J and Eisen O (2017) Critical porosity of gas enclosure in polar firn independent of climate. *Climate of the Past* **13**, 1685–1693.

Schlegel R and 8 others (2019) Comparison of elastic moduli from seismic diving-wave and ice-core microstructure analysis in Antarctic polar firn. *Annals of Glaciology* **60**(79), 220–230.

Schneebeli M (2004) Numerical simulation of elastic stress in the microstructure of snow. *Annals of Glaciology* **38**, 339–342.

Schoenberg M (1980) Elastic wave behavior across linear slip interfaces. *The Journal of the Acoustical Society of America* **68**(5), 1516–1521.

Schwander J, Stauffer B and Sigg A (1988) Air mixing in firn and the age of the air at pore close-off. *Annals of Glaciology* **10**, 141–145.

Shapiro LH, Johnson JB, Sturm M and Blaisdell GL (1997) Snow Mechanics: Review of the State of Knowledge and Applications. Technical report, Cold Regions Research and Engineering Lab, Hanover, NH.

Sidler R (2015) A porosity-based Biot model for acoustic waves in snow. *Journal of Glaciology* **61**(228), 789–798.

Smith JL (1965) The elastic constants, strength and density of Greenland snow as determined from measurements of sonic wave velocity. *CREEL Technical Report* **167**, 1–15.

Srivastava PK, Chandel C, Mahajan P and Pankaj P (2016) Prediction of anisotropic elastic properties of snow from its microstructure. *Cold Regions Science and Technology* **125**, 85–100.

Srivastava PK, Mahajan P, Satyawali PK and Kumar V (2010) Observation of temperature gradient metamorphism in snow by X-ray computed microtomography: measurement of microstructure parameters and simulation of linear elastic properties. *Annals of Glaciology* **51**(54), 73–82.

Stauffer B, Schwander J and Oeschger H (1985) Enclosure of air during metamorphosis of dry firn to ice. *Annals of Glaciology* **6**, 108–112.

Suriñach E, Vilajosana I, Khazaradze G, Biescas B, Furdada G and Vilaplana JM and 5 others (2005) Seismic detection and characterization of landslides and other mass movements. *Natural Hazards and Earth System Sciences* **5**(6), 791–798.

Van Herwijnen A and Schweizer J (2011) Monitoring avalanche activity using a seismic sensor. *Cold Regions Science and Technology* **69**(2-3), 165–176.

Voigt W (1910) *Lehrbuch der kristallphysik: (mit ausschluss der kristalloptik)*, vol. **34**. Leipzig: BG Teubner.

Wang X and Baker I (2013) Observation of the microstructural evolution of snow under uniaxial compression using X-ray computed microtomography. *Journal of Geophysical Research: Atmospheres* **118**(22), 12–371.

Wautier A, Geindreau C and Flin F (2015) Linking snow microstructure to its macroscopic elastic stiffness tensor: a numerical homogenization method and its application to 3-D images from X-ray tomography. *Geophysical Research Letters* **42**(19), 8031–8041.

Yamada T, Hasemi T, Izumi K and Sata A (1974) On the dependencies of the velocities of p and s waves and thermal conductivity of snow upon the texture of snow. *Contributions from the Institute of Low Temperature Sciences, Series A* **32**, 71–80.

Zimmerman RW (1990) *Compressibility of Sandstones*. Amsterdam: Elsevier.

https://doi.org/10.1017/jog.2021.25 Published online by Cambridge University Press

Appendix A.

Velocities in the high frequency limit of Biot theory

It is convenient to denote porosity by ϕ, density and bulk modulus of the solid (ice) by ρ_s and K_s, density and bulk modulus of the fluid (air) by ρ_f and K_f, and bulk and shear moduli of the ice frame by K_b and μ_b. In the high frequency limit, the *P*- and *S*-wave velocities are non-dispersive and are given by Johnson (1982*a*) as:

$$V_S^2 = \frac{\mu_b}{(1-\phi)\rho_s + (1-1/\tau)\phi\rho_f}, \tag{A.1}$$

$$V_{P,\text{fast, slow}}^2 = \frac{\Delta \pm \sqrt{\Delta^2 - 4(\rho_{11}\rho_{22} - \rho_{12}^2)(PR - Q^2)}}{2(\rho_{11}\rho_{22} - \rho_{12}^2)}. \tag{A.2}$$

In these equations, $\tau > 1$ is a geometrical quantity related to the tortuosity of the pore space in terms of which:

$$\rho_{11} = (1-\phi)\rho_s + (\tau - 1)\phi\rho_f, \tag{A.3}$$

$$\rho_{12} = (1-\tau)\phi\rho_f, \tag{A.4}$$

$$\rho_{22} = \phi\rho_f + (\tau - 1)\phi\rho_f. \tag{A.5}$$

The quantities *P*, *Q* and *R* are given by:

$$P = \frac{(1-\phi)(1-\phi-K_b/K_s)K_s + \phi K_s K_b/K_f}{1-\phi-K_b/K_s+\phi K_s/K_f} + \frac{4\mu_b}{3}, \tag{A.6}$$

$$Q = \frac{(1-\phi-K_b/K_s)\phi K_s}{1-\phi-K_b/K_s+\phi K_s/K_f}, \tag{A.7}$$

$$R = \frac{\phi^2 K_s}{1-\phi-K_b/K_s+\phi K_s/K_f}, \tag{A.8}$$

The quantity Δ is defined by:

$$\Delta = P\rho_{22} + R\rho_{11} - 2Q\rho_{12}. \tag{A.9}$$

https://doi.org/10.1017/jog.2021.25 Published online by Cambridge University Press